Article

In vivo imaging of senescent vascular cells in atherosclerotic mice using a #-galactosidase-activatable nanoprobe

Ji-An Chen, Wei Guo, Zhijun Wang, Nannan Sun, Hongming Pan, Jiahui Tan, Zhirong Ouyang, Wei Fu, Yonghui Wang, Wei Hu, and Xianfeng Gu

Anal. Chem., **Just Accepted Manuscript** • DOI: 10.1021/acs.analchem.0c02670 • Publication Date (Web): 10 Aug 2020

In vivo imaging of senescent vascular cells in atherosclerotic mice using a *β*-galactosidase-activatable nanoprobe

Ji-An Chen[a‡], Wei Guo[a‡], Zhijun Wang[a], Nannan Sun[a], Hongming Pan[a], Jiahui Tan[a], Zhirong Ouyang[a], Wei Fu[a], Yonghui Wang[a], Wei Hu[a*], Xianfeng Gu[a*]

[a] School of Pharmacy & Minhang Hospital, Fudan University, Shanghai 201301, China

*Corresponding author: xfgu@fudan.edu.cn; 18918169120@163.com

ABSTRACT: Senescence-associated diseases have severely diminished the quality of life and health of patients. However, a sensitive assay of these diseases remains limited due to a lack of straightforward methods. Considering that senescence-associated *β*-galactosidase (SA-*β*-Gal) is overexpressed in senescent cells, the detection of SA-*β*-Gal in senescent cells and tissues might be a feasible strategy for the early diagnosis of the SA diseases. In this study, a *β*-galactosidase-activatable nanoprobe **BOD-L-*β*Gal-NPs** was developed for the imaging of senescent cells and vasculature in atherosclerotic mice via real-time monitoring of *β*-Gal. **BOD-L-*β*Gal-NPs** was fabricated by encapsulating a newly designed NIR ratiometric probe **BOD-L-*β*Gal** within a poly(lactic-co-glycolic) acid (PLGA) core. Nanoprobe **BOD-L-*β*Gal-NPs** showed good accumulation in arteries, thus successfully visualizing senescent cells and vasculature in atherosclerotic mice by tail vein injection. Our findings indicated that nanoprobe **BOD-L-*β*Gal-NPs** hold great potential for the early diagnosis and therapy of atherosclerosis and other aging-associated diseases.

Aging-associated diseases have become one of the major social problems with an increasingly aging population.[1–4] Therefore, the early diagnosis of aging-associated diseases is crucially needed. Cell senescence, which has emerged as a potentially important contributor to aging-related diseases, is manifested as an irreversible arrest in cell proliferation in response to various types of stress.[5–8] Thus, imaging and detecting senescent cells is of great significance for the early diagnosis of aging-related diseases.

Atherosclerosis is an aging-related disease that has become a major cause of mortality and morbidity worldwide because atherosclerotic plaques could lead to potentially catastrophic outcomes such as stroke and myocardial infarction (MI).[9–15] The development of new therapies for atherosclerosis could be facilitated by imaging assays that provide anatomic information with high spatial and temporal resolution. Currently, several methods, such as microscopic computed tomography (micro-CT),[16, 17] magnetic resonance imaging (MRI)[18] and Doppler measurements by micro-ultrasonography,[19, 20] have been developed to image vascular structures and hemodynamics. However, these imaging methods have several limitations, including long scanning and postprocessing times and attenuated spatial resolution with increased depth of penetration. Owing to its high temporal and spatial resolution, deep tissue penetration, and minimum interference from background autofluorescence by biomolecules in living systems,[21–28] near-infrared (NIR) fluorescence-based imaging has significant advantages over tomographic imaging. Fluorescence-based vascular imaging can be achieved by specific recognition and a reaction between fluorescent probes and cells or biomolecules in the vasculature. Increasing evidence has demonstrated that the senescence of vascular smooth muscle cells (VSMCs) and endothelial cells (ECs) plays a crucial role in the pathogenesis of atherosclerosis.[12, 13, 29–32] Thus, the detection of senescent cells in arterial tissue based on NIR fluorescence technology might be a feasible strategy for imaging and the early diagnosis of atherosclerotic vasculature.

Considering that senescence-associated *β*-galactosidase (SA-*β*-Gal) is overexpressed in senescent cells, an NIR fluorescent probe for *β*-Gal could be a promising tool for the selective detection of senescent cells.[33, 34] Although several fluorescent probes have been reported for the visualization of senescent cells by detecting the activities of *β*-Gal,[35–38] to the best of our knowledge, *in vivo* imaging of senescent cells in pathological vasculature has not been achieved. Since arteries are typically located among deep tissues *in vivo*, deep tissue penetration of the probe is necessary for imaging arteries. Moreover, a high blood flow speed in arteries causes difficulties in uptake of small molecular probes by vascular cells, and the probe might hardly accumulate in arteries. Most importantly, a small molecular probe is inevitably metabolized *in vivo,* further hindering the probe from reaching the target tissue. The aforementioned concerns prompted us to create a *β*-galactosidase-activatable nanoprobe for imaging atherosclerotic vasculature *in vivo* by detecting *β*-Gal in senescent VSMCs. To prove this concept, we first developed a small molecule-based NIR probe (**BOD-L-*β*Gal**) by incorporating *β*-galactose residues into boron dipyrromethene (BODIPY) fluorophore via a self-elimination linker. **BOD-L-*β*Gal** showed a fast ratiometric and turn-on fluorescence response to *β*-Gal *in vitro*. As expected, the ratiometric NIR fluorescent probe **BOD-L-*β*Gal** enabled fast detection of *β*-Gal in senescent VSMCs induced by angiotensin II with a high signal-to-noise ratio. However, after directly injecting **BOD-L-*β*Gal** via the tail vein, imaging of senescent cells was not ideal in atherosclerotic mice (ApoE$^{-/-}$ mice induced by angiotensin II), possibly due to the poor uptake of **BOD-L-*β*Gal** by the vascular cells of the atherosclerotic mice and the fast metabolism of the probe.

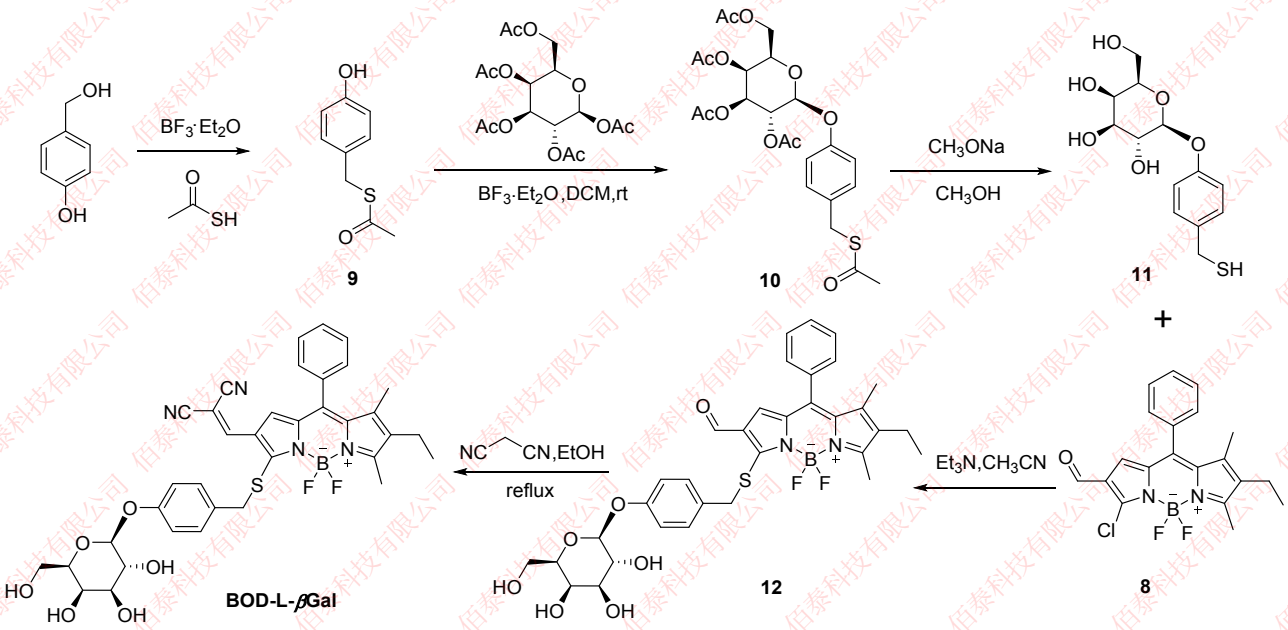

Scheme 1. The Synthesis of BOD-L-*β*Gal

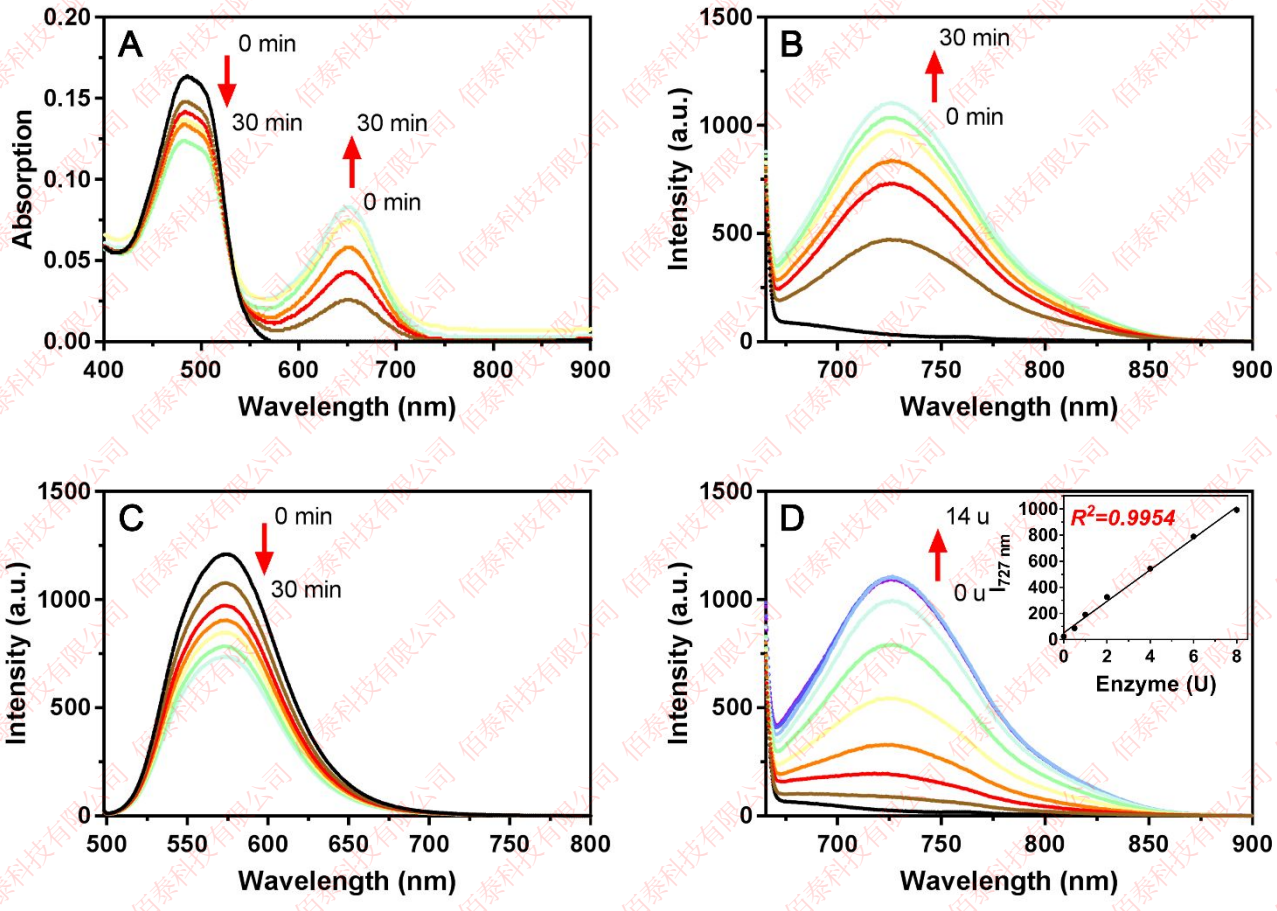

Figure 1. Absorption and fluorescence responses of **BOD-L-*β*Gal** to *β*-gal. **BOD-L-*β*Gal** (10 μM) incubation with *β*-gal (14 U) in aqueous solution (PBS:DMSO = 7:3 v:v, pH = 7.4, 37 °C). (A) Time dependence of the absorption spectra (0-30 min). (B) Time dependence of the fluorescence spectra (0-30 min), λ_{ex} = 651 nm. (C) Time dependence of the fluorescence spectra (0-30 min), λ_{ex} = 488 nm. (D) The emission spectra of **BOD-L-*β*Gal** upon the addition of *β*-gal (0-14 U), λ_{ex} = 651 nm. Inset: The relationship between I_{727} nm and the *β*-gal concentration. The detection limit of **BOD-L-*β*Gal** was 0.014 U/mL.

To overcome these issues, nanoprobe **BOD-L-*β*Gal-NPs** was fabricated by incorporating **BOD-L-*β*Gal** into polymer nanoparticles consisting of poly(lactic-co-glycolic) acid (PLGA) that has been reported to be taken up by a variety of vascular cells, such as VSMCs, ECs and monocytes.[39, 40] As we hypothesized, nanoprobe **BOD-L-*β*Gal-NPs** successfully visualized the atherosclerotic vasculature in ApoE$^{-/-}$ mice after intravenous administration. To the best of our knowledge, **BOD-L-*β*Gal-NPs** is the first probe that is suitable for *in vivo* imaging senescent cells and vasculature in atherosclerosis.

EXPRIMENTAL SECTION

General Information. All commercially available solvents and chemicals were used without further purification unless special stated. 1H NMR and 13C spectra were recorded on a Bruker AV-400 and AV 600 MHz instruments with chemical shifts reported in ppm. Deuterated chloroform and Deuterated DMSO were used as the solvent, TMS as the internal standard. Mass spectra were measured on an HP 1100 LC-MS spectrometer.

Synthesis of compound BOD-L-*β*Gal. Compound **12** (300mg, 0.46 mmol) was dissolved in freshly distilled EtOH (20 mL), followed by the addition of malononitrile (92 mg, 1.38 mmol). The solution was stirred for 5 h at 90 °C under argon. After cooling to room temperature, the solvent was removed *in vacuo* and the residue was purified by silica gel column (DCM: MeOH = 15: 1) to afford **BOD-L-*β*Gal** (150mg, 46.5%). ^{1}H NMR (400 MHz, DMSO-d_6) δ 7.65 – 7.41 (m, 6H), 7.02 (d, J = 8.3 Hz, 2H), 6.92 (d, J = 8.0 Hz, 2H), 6.81 (s, 1H), 5.15 (m, 1H), 4.91 (m, 1H), 4.76 (m, 1H), 4.64 (m, 1H), 4.53 (m, 1H), 4.11 (m, 2H), 3.52 (m, 4H), 2.73 (s, 3H), 2.43 (q, J = 7.4 Hz, 2H), 1.49 (s, 3H), 1.01 (s, J = 7.4 Hz, 3H). ^{12}C NMR (151 MHz, DMSO-d_6), δ 171.13, 157.31, 151.45, 145.10, 144.28, 140.12, 138.94, 137.05, 136.21, 131.95, 130.27, 130.15, 129.92, 129.68, 128.85, 128.80, 127.10, 118.92, 116.46, 114.51, 113.49, 101.53, 75.44, 73.31, 70.25, 67.95, 62.81, 60.13, 41.25, 40.05, 39.52, 16.57, 14.05, 13.61, 12.37. HRMS (ESI, m/z): calculated for $C_{36}H_{35}BF_2N_4NaO_6S^+$ [M+Na]$^+$: 723.2231, found: 723.2222.

***In vitro* enzymatic assay. BOD-L-*β*Gal** was used at a final concentration of 10 μM. Absorption and fluorescence spectra of **BOD-L-*β*Gal** with *β*-gal enzymatic reactions were performed at 37 °C in a 3 mL total volume of PBS buffer (0.1 M, pH 7.4, 30% DMSO) in a 1 cm cuvette. UV–vis absorption spectra were recorded on U-2900 Spectrophotometer (Hitachi, Japan). Fluorescence spectra were measured with F-7000 Fluorescence Spectrophotometer (Hitachi, Japan).

Preparation of PLGA Nanoparticles. Poly(lactic-co-glycolic acid) (PLGA) polymer with an average molecular weight of 20,000 and a lactide-to-glycolide copolymer ratio of 75:25 (Jinan Daigang Biomaterial Co., China) was used to prepare the nanoparticles. PLGA (100 mg) was dissolved completely in 2 mL acetone and 1 mL methanol. Then, **BOD-L-*β*Gal** was added to this solution. The resultant organic solution was emulsified into 25 mL of an aqueous PVA solution (1.0%, w/v) and stirred at 400 rpm using a propeller-type agitator with 3 blades for 30 min. After the mixture was agitated for 2 h under reduced pressure at 40 °C, the entire dispersed system was then centrifuged (43,400 × g for 10 min at -20 °C, Hitachi CP-100NX, Japan), resuspended in distilled water and centrifuged again to remove excess polyvinyl alcohol and the unencapsulated reagent that could not absorb onto the surfaces of the nanoparticles. After the process was repeated, the resultant dispersion was dried using a freeze drying method. The encapsulation efficiency (EE) and loading capacity (LC) of **BOD-L-*β*Gal-NPs** were qualified by a HPLC system (Agilent 1200, USA) after the samples were demulsified by acetone. The EE and LC of **BOD-L-*β*Gal** in **BOD-L-*β*Gal-NPs** were approximately 55.78 ± 4.88% and 9.69 ± 0.84% (w/w), respectively. The average diameters of the **BOD-L-*β*Gal-NPs** were 153.2 ± 6.5 nm, the PdI is 0.123 and the surface charges (zeta potential) analyzed by Zetasizer Nano (Malvern ZEN 3600 Zetasizer Nano System) were -18.7 ± 0.3 mV.

The culture of primary rat vascular smooth muscle cells (VSMCs). Male Sprague Dawley (SD), 80-100g, were anesthetized with sodium pentobarbital (40 mg/kg, Sigma). The isolated VSMCs were cultured in Dulbecco's modified Eagle's medium (DMEM, HyClone) supplemented with 10% fetal bovine serum (FBS, Gibco), 1% penicillin-streptomycin (Gibco), and were used at bioimaging.

***In vitro* cytotoxicity assay.** The cytotoxicity of **BOD-L-*β*Gal** and **BOD-L-*β*Gal-NPs** towards VSMCs was measured by the cell counting kit-8 (CCK-8 kit, Beyotime Biotechnology, Jiangsu, China). Briefly, VSMCs were plated in 96 well plates at a density of 5,000 cells/well in 0.1 mL volume of serum-free culture media. The following day, cells were treated with desired concentrations of **BOD-L-*β*Gal** or **BOD-L-*β*Gal-NPs**. After incubation for 24 h, 10 μl CCK-8 solution was added to each well, then, the absorbance was measured at 450 nm with a microplate reader (Varioskan Flash Multimode Reader, Thermo Scientific, USA). Data were collected in three independent experiments.

Fluorescence imaging under the senescent condition. VSMCs were plated in Glass Bottom Cell Culture Dish (NEST) at a density of 8×10^4 cells/mL. After cultures reached confluence in growth medium, VSMCs were transferred to serum-free medium and incubated with Ang II at 5 μM for 3 days. Since Ang II, a peptide drug, is easily degraded, the growth medium should be refreshed every 12 h. VSMCs untreated with Ang II cultured with serum-free medium and cells cultured with serum-containing medium were used as controls. After 3 days, all cells were washed and incubated in serum-free medium containing 10 μM of **BOD-L-*β*Gal** for 1 h. Live cell images were acquired using Carl Zeiss LSM710 with a 20 × objective. Green fluorescence was excited at 488 nm and emission was collected at 569-623 nm. Red fluorescence was excited at 561 nm and emission was collected at 698-754 nm.

Animals experimental protocol. At 12 weeks of age, mice began receiving the high-fat diet (Research Diets, USA). After 4 weeks of high-fat diet, all mice were infused with angiotensin II dissolved in PBS at 1.44 $mg \cdot kg^{-1} \cdot d^{-1}$ via an osmotic mini-pump for 4 weeks. Mice were anesthetized with intraperitoneal injection of pentobarbital at day 28 of angiotensin II infusion for imaging. Male C57BL/6 mice, received normal rodent chow and did not treated with angiotensin II, used as control.

Real-time *in vivo* imaging in senescent mice. At day 28 of angiotensin II infusion, *in vivo* fluorescence imaging in angiotensin II-infused mice was performed at 24 h, following intravenous injection of **BOD-L-*β*Gal** (300 μL, 3.3 mg/mL) or **BOD-L-*β*Gal-NPs** (300 μL, 33.3 mg/mL), using an *in vivo* fluorescence imaging system (VISQUE InVivo Smart, Republic of Korea) by Cy5.5 model (Ex: 630-680 nm, Em: 690-740 nm). Whole-body images were obtained from an

anesthetized epilatory mouse and analyzed with CleVue software.

***Ex vivo* imaging of different sections of fresh organs after BOD-L-*β*Gal or BOD-L-*β*Gal-NPs treatment.** For *ex vivo* imaging, mice, following intravenous injection of **BOD-L-*β*Gal** (300 μL, 3.3 mg/mL) or **BOD-L-*β*Gal-NPs** (300 μL, 33.3 mg/mL), were euthanized with intraperitoneal injection of pentobarbital, and organs were analyzed immediately after harvesting. Fluorescence images were taken on VISQUE InVivo Smart by using Cy5.5 model (Ex: 630-680 nm, Em: 690-740 nm).

RESULTS AND DISCUSSION

To detect senescent cells, a NIR fluorescent probe, **BOD-L-*β*Gal**, was developed. The **BOD-L-*β*Gal** probe integrated a *β*-galactose residue as a responsive site with a BODIPY-based NIR fluorophore via a self-elimination linker (Scheme 1). Two cyano groups (electron-withdrawing groups) were specifically incorporated through a vinylene bridge into the BODIPY core to provide fluorescence in the NIR region. **BOD-L-*β*Gal** was readily synthesized in two steps beginning with 2-chloro-3-formyl-5,7-dimethyl-6-ethyl-8-phenyl-BODIPY **8** and 6-(4-mercaptomethyl-phenoxy)-*β*-galactose **11**, which were prepared according to a previously reported method (Scheme S1).[41] All compounds were characterized and identified by high-resolution mass spectrometry (HRMS), ^{1}H NMR and ^{13}C NMR.

After synthesizing **BOD-L-*β*Gal**, we initially explored the ability of **BOD-L-*β*Gal** to detect *β*-Gal *in vitro*. The optical properties of **BOD-L-*β*Gal** in the absence and presence of *β*-Gal were evaluated in aqueous solution (phosphate-buffered saline (PBS): dimethyl sulfoxide (DMSO) = 7:3 v:v, pH = 7.4, 37 °C). As shown in the absorption spectra, *β*-Gal immediately caused a new peak to appear at approximately 650 nm, which was accompanied by a decrease in the absorption at 500 nm (Figure 1A). In the absence of *β*-Gal, the probe was fluorescent with a maximum peak at 580 nm (λ_{em}=488 nm). In contrast, in the presence of *β*-Gal, the **BOD-L-*β*Gal** probe immediately caused a strong fluorescence signal to appear in the NIR region with a maximum peak at approximately 730 nm (Figure 1B, λ_{em} = 651 nm) along with a remarkable decrease in the fluorescence intensity at 580 nm (Figure 1C, λ_{em}=488 nm), indicating the ability of **BOD-L-*β*Gal** to serve as a dual-channel ratiometric sensor for *β*-Gal. The fluorescence titration experiments demonstrated that **BOD-L-*β*Gal** enabled the assay of *β*-Gal by both ratiometric and turn-on NIR fluorescence modes with a calculated detection limit of 0.014 U/mL (Figure 1D).

Considering that the **BOD-L-*β*Gal** probe showed distinct ratiometric and turn-on NIR fluorescence response behaviors to *β*-Gal, we evaluated the selectivity of **BOD-L-*β*Gal** for *β*-Gal over various related enzymes and ions by monitoring the change in the fluorescence ratio (I_{730}/I_{580}) and fluorescence intensity in the NIR region (approximately 730 nm). As shown in Figure S1, obvious changes were only observed under the treatment of *β*-Gal, indicating that **BOD-L-*β*Gal** has high selectivity for *β*-Gal with both ratiometric and turn-on NIR fluorescence responses.

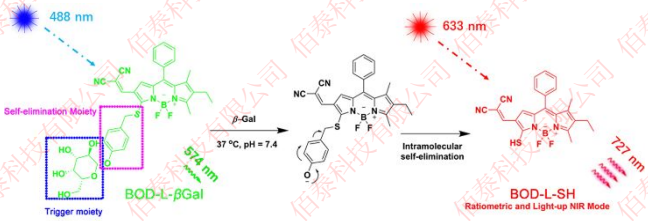

Scheme 2. The Proposed Sensing Mechanism for *β*-Gal Enzymatic Activation of BOD-L-*β*Gal

Based on the abovementioned results of the optical properties and sensing selectivity of **BOD-L-*β*Gal**, we deduced that the distinct fluorescence responses of **BOD-L-*β*Gal** to *β*-Gal were caused by the hydrolyzation of *β*-glucose residues from **BOD-L-*β*Gal** catalyzed by *β*-Gal, which subsequently underwent linker self-elimination to release a BODIPY-based NIR fluorophore (Scheme 2). Our proposed sensing mechanism of **BOD-L-*β*Gal** to *β*-Gal was further verified by HRMS analysis of the product from this enzymatic reaction (Figure S2), the HRMS analysis only indicated the peak of a thiol-substituted product. This result suggested that the *β*-glucose residue and linker were both removed, which was in agreement with our proposed mechanism.

To understand the relationship between the probe structure and *β*-Gal detection ability, docking calculations were carried out for **BOD-L-*β*Gal** with *β*-Gal. The active site architecture showing the interactions between the **BOD-L-*β*Gal** and *β*-Gal pocket was performed using the Schrodinger 3.5 software package. The protein assigned for the docking analysis was *E. coli* *β*-Gal (PDB ID 1JYN). The binding mode of our probe molecule was explored on the basis of on the previously mentioned structural information. The docking of **BOD-L-*β*Gal** in the *β*-Gal pocket revealed the binding mode of a typical *β*-Gal substrate (Figure 2). The galactosyl moiety of **BOD-L-*β*Gal** forms hydrogen bonds with His540 (2.75), Gln537 (3.08), Glu461 (2.66, 3.03 and 3.46), Asp201 (2.78) and Asn102 (3.98) as the lactose molecule is produced, while the fluorescent group BODIPY is out of the active binding site, thereby not affecting hydrolysis. An overlay of **BOD-L-*β*Gal** with the previously reported natural substrate lactose in the *β*-Gal cocrystal structure (PDB ID 1JYN) indicated that the galactosyl moiety occupied nearly the same location of lactose and maintained a conservative interaction with *β*-Gal; thus, **BOD-L-*β*Gal** is a good substrate of *β*-Gal (Figure 2).

Because **BOD-L-*β*Gal** has the ability to detect *β*-Gal with distinct fluorescence patterns, we next applied this probe for imaging senescent cells. The selective detection of senescent cells was carried out by using confocal fluorescence imaging. Ratiometric fluorescence probes have considerable practical advantages over probes with a single-wavelength fluorescence response because they can exhibit a spectral fluorescence signal shift upon reacting with an analyte; thus, the detectable ratio signal can be obtained by two independent read-out channels of reacted versus unreacted probes, resulting in improved and reliable signal quantification.[26, 28, 42–49] Since **BOD-L-*β*Gal** serves as a ratiometric fluorescence probe for monitoring *β*-Gal, we explored the ability of **BOD-L-*β*Gal** to detect senescent cells in a dual-color manner.

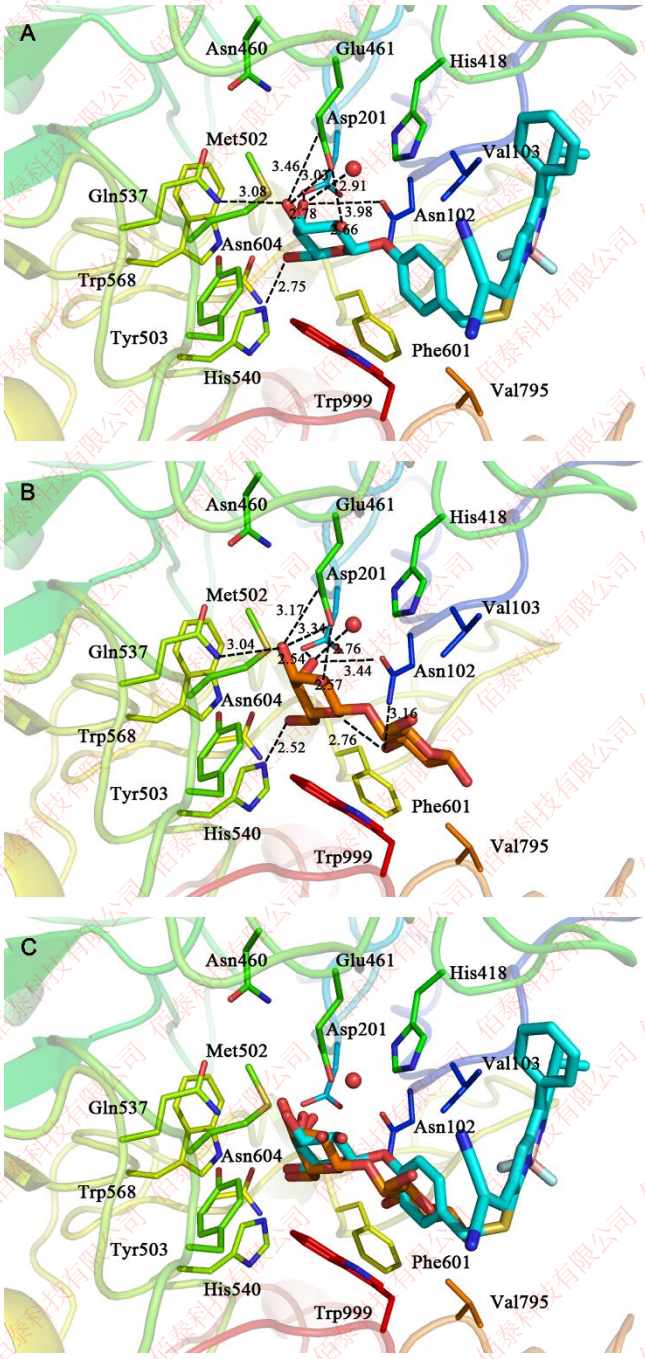

Figure 2. Docking mode of **BOD-L-*β*Gal** (A), lactose (B) with *β*-Gal. Docking mode of **BOD-L-*β*Gal** (blue, sticks), lactose (orange, sticks) with *β*-Gal (rainbow, cartoon, PDB ID 1JYN). Hydrogen bonds are illustrated as cyan dotted lines; (C)Aligned structures of lactose (orange, sticks) and **BOD-L-*β*Gal** (blue, sticks) in *β*-Gal binding pocket (rainbow, cartoon, PDB ID 1JYN).

As shown in Figure 3, the strongest fluorescence signals in the red channel (698-759 nm) and weakest fluorescence signals in the green channel (569-623 nm) were observed in the group of senescent VSMCs induced by Ang II, and the fluorescence ratio (I_{red}:I_{green}) was approximately 4.8. In contrast, the strongest green emission and weakest red emission were observed in the groups of primary VSMCs, and the fluorescence ratio (I_{red}:I_{green}) was only 0.4. In the group of VSMCs cultured without serum, an intermediate fluorescence ratio (1.5) was obtained. All these imaging experiments indicated that **BOD-L-*β*Gal** is capable of discriminating senescent VSMCs from normal VSMCs. To further confirm that the significant ratiometric fluorescence signal induced by *β*-Gal was indeed from senescent cells, two traditional experiments for analyzing *β*-Gal in cells (cell staining by X-Gal and western blot) were also carried out. X-Gal, which is a commonly used dye for detecting *β*-Gal in cells, stains cells blue after X-Gal reacts with *β*-Gal. However, the X-Gal assay method is not suitable for live cell imaging because cell fixation is required before staining. As shown in Figure 3, the X-Gal staining and western blot results are in good agreement with the results obtained by **BOD-L-*β*Gal**. The results demonstrated that **BOD-L-*β*Gal** can be applied for real-time imaging of *β*-Gal in senescent cells. In addition, the *in vitro* cytotoxicity of the probe was evaluated with VSMCs using a cell counting kit-8 (CCK-8) assay. **BOD-L-*β*Gal** did not show obvious adverse effects on VSMC cell viability, indicating good biocompatibility (Figure S3A). As we know there is an inevitable link between apoptosis and senescence, we perform the co-staining experiments of Hoechst 33258 and **BOD-L-*β*Gal** (Figure S11). The results indicated that **BOD-L-*β*Gal** is not sensitive to the apoptotic cells, whether the apoptotic cells among normal cells or senescent cells.

Encouraged by the results from imaging senescent cells *in vitro*, we finally aimed to *in vivo* fluorescence imaging of Senescent Cells. Atherosclerosis is an aging-associated disease that is caused by long-term dyslipidemia and greatly affects the quality of life and health of patients. Thus, the early diagnosis and effective therapy of atherosclerosis are urgently needed. Importantly, an increasing number of studies have demonstrated that atherosclerotic vascular cells exhibit obvious features of cellular senescence,[9, 15] providing opportunities for the early diagnosis of atherosclerosis by using probes for senescent cells. First, we explored the application of **BOD-L-*β*Gal** to imaging the atherosclerotic vasculature *in vivo*. $ApoE^{-/-}$ mice pretreated with Ang II for 4 weeks were used as an animal model of atherosclerosis, and the $ApoE^{-/-}$ mice without the Ang II pretreatment were used as controls. After caudal vein injection of the **BOD-L-*β*Gal** probe, a marked difference between the atherosclerotic mice and control mice was not observed in the images of the live mice and in the aortic arch dissected from the mice (Figure S4). We speculated that unideal images might result from ineffective accumulation of the **BOD-L-*β*Gal** probe in vascular cells due to a high blood flow speed in arteries and the fast metabolism of the probe *in vivo*.

It has been reported that nanoparticles formulated with poly(lactic-co-glycolic) acid (PLGA) are easily taken up by a variety of vascular cells, such as VSMCs, ECs and monocytes, after intravenous administration. However, PLGA-based nanoprobes for the imaging of senescent cells in a living mouse model have not been previously developed. In this study, to improve the selective cellular uptake of imaging probes in vascular cells during *in vivo* imaging, a nanoprobe **BOD-L-*β*Gal-NPs** was prepared by encapsulating **BOD-L-*β*Gal** within the interior of PLGA nanoparticles. Transmission electron micrograph (Figure S5B) showed that **BOD-L-*β*Gal-NPs** had an average of ~100 nm in diameter, while results form dynamic light scattering analysis were a bit larger (153.2 ± 6.5 nm). The time-release profile demonstrated that less than 10% **BOD-L-*β*Gal** was released form **BOD-L-*β*Gal-NPs** in

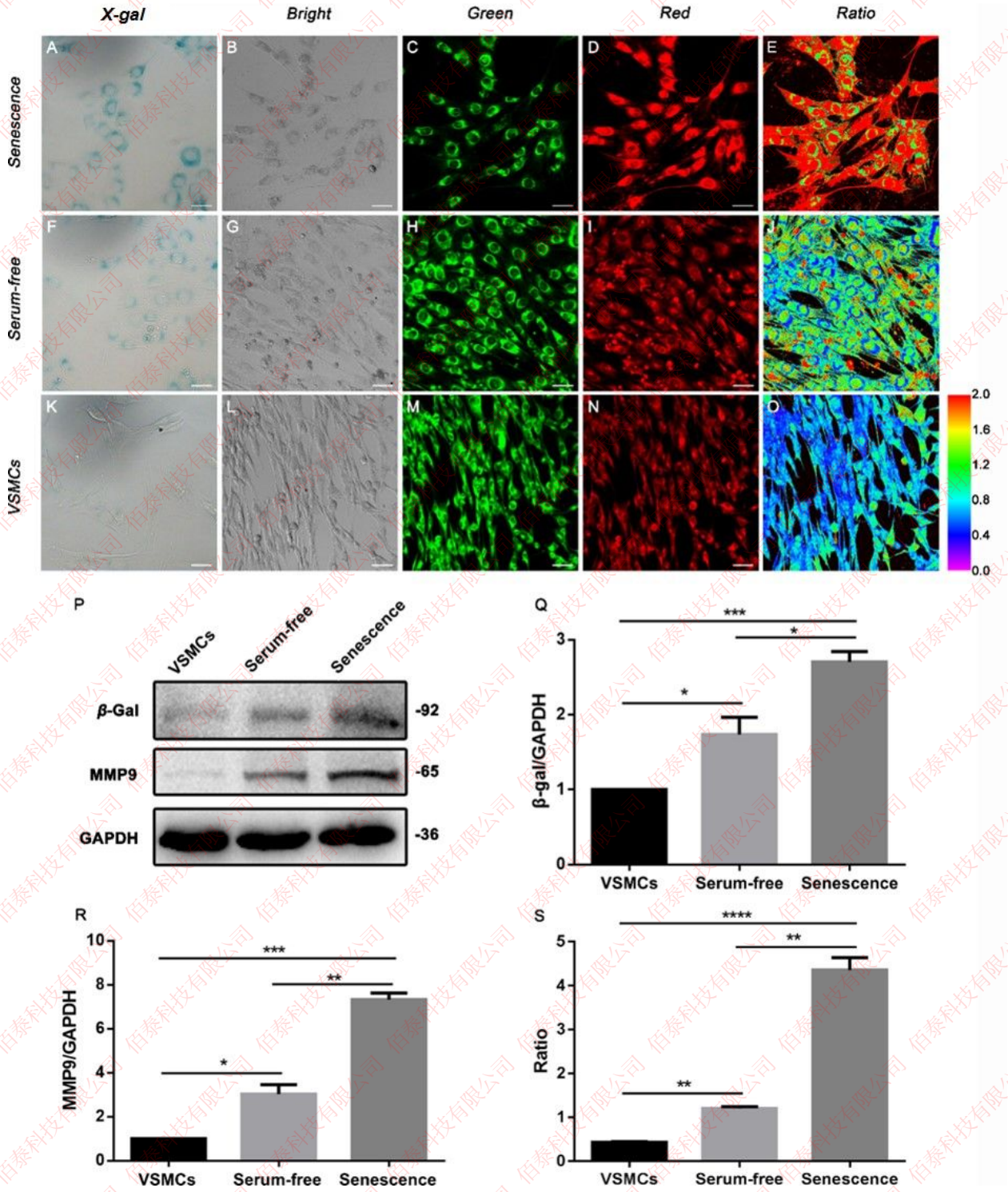

Figure 3. Confocal images and western blotting analysis of VSMCs.

The imaging of Ang II-treated VSMCs (A-D), serum-free-treated VSMCs (F-I) and primary VSMCs (K-N) using **BOD-L-*β*Gal** (10 μM) for 1 h (3th-4th column) and X-gal (1st column). The green channel was obtained from 569 to 623 nm (λ_{ex} = 488 nm), and the red channel was obtained from 698 to 759 nm (λ_{ex} = 633 nm). Ratiometric images (5th column) of Ang II-treated VSMCs (E), serum-free-treated VSMCs (J) and primary VSMCs (O) generated from the red channel to green channel. Western blotting analysis showed that Ang II significantly upregulated the expression of the senescence-associated proteins *β*-Gal and MMP9 in Ang II-treated VSMCs (P, Q, R). Semiquantitative determination of SA-*β*-Gal activity in Ang II-treated VSMCs, serum-free-treated VSMCs and primary VSMCs according to the ratio of the average fluorescence intensity of the red channel to the green channel (S). The error bars represent the standard deviation (S.D.). Scale bar = 50 μm. The experiments were performed three times. (∗) $p < 0.05$, (∗∗) $p < 0.01$, (∗∗∗) $p < 0.001$, and (∗∗∗∗) $p < 0.0001$ compared to the control group.

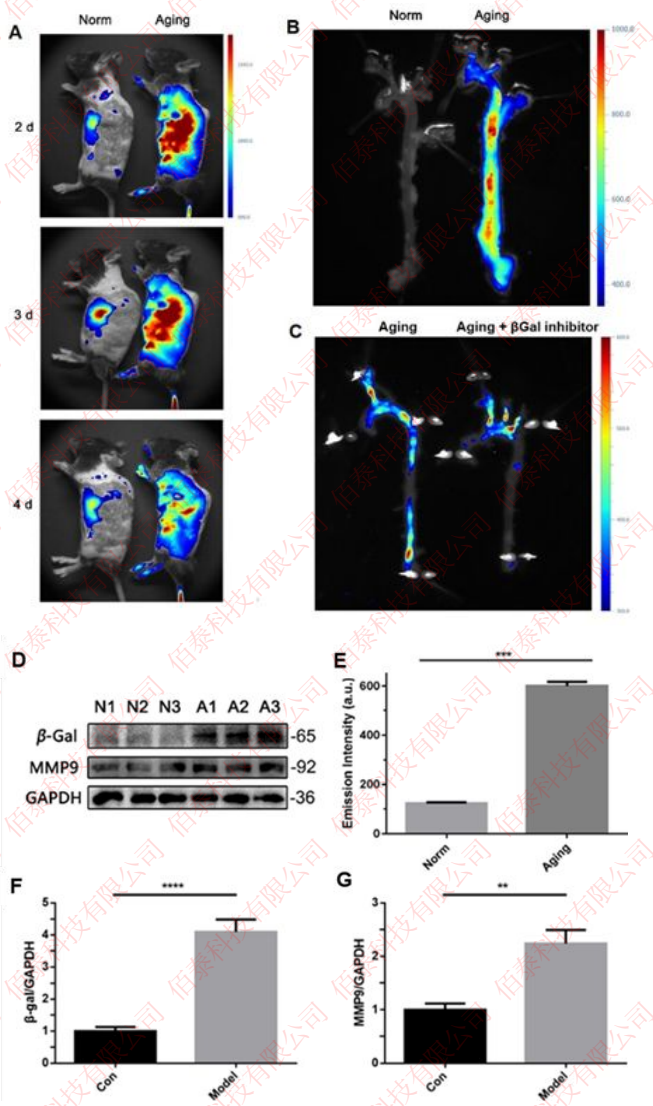

Figure 4. Fluorescence imaging and western blotting analysis of atherosclerotic mice and control mice. Time-based *in vivo* fluorescence imaging of atherosclerotic mice ($ApoE^{-/-}$ mice pretreated with Ang II) and control mice ($ApoE^{-/-}$ mice without the treatment of Ang II) after injecting **BOD-L-*β*Gal-NPs** (300 μL, 33.3 mg/mL) via intravenous injection (A). Fluorescence images of the aortic arch of an Ang II-treated mouse and control after the injection of **BOD-L-*β*Gal-NPs** for 1 day (B). Fluorescence imaging of atherosclerotic mice treated with **BOD-L-*β*Gal-NPs** or **BOD-L-*β*Gal-NPs** +Inhibitor-NPs via intravenous injection for 1 day (C). Western blotting analysis showed that Ang II significantly upregulated the expression of the senescence-associated proteins *β*-Gal and MMP9 in the aortic arches of three Ang II-treated mice (A1-A3) compared with three control mice (N1-N3) (D). The values were normalized to the control (1.0) (E, F). Semiquantitative analysis of SA-*β*-Gal activity in the aortic arch according to the emission intensity (G). The error bars represent the S.D. The experiments were performed three times. (∗) $p < 0.05$, (∗∗) $p < 0.01$, (∗∗∗) $p < 0.001$, and (∗∗∗∗) $p < 0.0001$ compared to the control group.

PBS within 7 days (Figure S5C). The size of **BOD-L-*β*Gal-NPs** generally remained unchanged after one-week incubation in both PBS buffer and 10% fetal bovine serum (Figure S5D). **BOD-L-*β*Gal-NPs** exhibited less cytotoxicity than **BOD-L-*β*Gal** to VSMCs following 24 h incubation (Figure S3B). These results suggested that **BOD-L-*β*Gal-NPs** had good biocompatibility and could be used to perform *in vivo* imaging. It was found that **BOD-L-*β*Gal** remained a dramatic optical response to *β*-Gal within the PLGA nanoparticles. As expected, a marked difference in the NIR fluorescence signal between the atherosclerotic mice and control mice was observed after the injection of **BOD-L-*β*Gal-NPs** via the caudal vein of $ApoE^{-/-}$ mice (Figure 4A). To further prove the capacity ability of **BOD-L-*β*Gal-NPs** to image senescent atherosclerotic vasculature, the mice were sacrificed humanely, and the aortic arch and some organs were dissected for fluorescent imaging (as shown in Figures 4B and S6). A significant fluorescence signal was observed in the aortic arch of the atherosclerotic mice after the preinjection of **BOD-L-*β*Gal-NPs** via the caudal vein, while a minimal signal was observed in the aortic arch of the control mice. These imaging results are in good accordance with the western blot, X-gal staining and Oil Red O staining results of the aortic arch (Figures 4D-G and S7, S8, S9). To validate that the fluorescent signals were indeed activated by *β*-Gal in senescent atherosclerotic vasculature, the atherosclerotic mice pre-treated with **BOD-L-*β*Gal-NPs** and *β*-Gal inhibitor **D-galactose-NPs** via intravenous injection for 1 day. The vascular imaging results showed that **D-galactose** effectively suppressed fluorescence signals caused by **BOD-L-*β*Gal-NPs** in senescent atherosclerotic vasculature (Figure 4C), which suggested that **BOD-L-*β*Gal-NPs** could be reliable tools for visualization of senescent atherosclerotic vasculature by detecting *β*-Gal activity. In addition, marked fluorescence signals were observed in the livers of the atherosclerotic mice and control mice, while stronger signals were observed in the livers of the atherosclerotic mice. This phenomenon might be due to metabolism of the probe in the liver and liver senescence in the atherosclerotic mice[50–52] which was confirmed by our western blot results (Figure S6) and the fluorescent images of the organs preinjection of *β*-Gal inhibitor **D-galactose-NPs** (Figure S10).

In summary, we successfully developed **BOD-L-*β*Gal**, which is a BODIPY-based NIR ratiometric probe, to detect senescent cells via the enzymatic reaction of *β*-Gal. The probe exhibited a great optical response to *β*-Gal with high sensitivity and selectivity. By exploiting these advantages, we successfully utilized the probe to detect senescent VSMCs *in vitro* in a ratiometric manner. To further investigate the ability of the probe to detect senescent cells *in vivo*, atherosclerotic mice were used as a senescent animal model. After failing to detect senescent vasculature and cells of atherosclerotic mice by a direct caudal vein injection of the **BOD-L-*β*Gal** probe, PLGA nanoparticles encapsulated with the **BOD-L-*β*Gal** probe were further developed to improve the up-take of the probe in vascular cells during *in vivo* imaging. As expected, our nanoparticles successfully imaged senescent cells and vasculature in the atherosclerotic mice. To the best of our knowledge, the **BOD-L-*β*Gal-NPs** probe is the first probe that is suitable for imaging senescent cells, vasculature and organs *in vivo*, indicating the great potential for the early diagnosis and therapy of atherosclerosis and other aging-associated diseases.

ASSOCIATED CONTENT

Supporting Information

The following files are available free of charge.

Detailed synthesis and characterization, experimental procedures, supplementary figures.

AUTHOR INFORMATION

Corresponding Author

*E-mail: xfgu@fudan.edu.cn ； 18918169120@163.com

Present Addresses

†If an author's address is different than the one given in the affiliation line, this information may be included here.

Author Contributions

‡These authors contributed equally.

Notes

The authors declare no competing financial interest.

ACKNOWLEDGMENT

This work was supported by the National Natural Science Foundation of China (No. 21572039, 21977018). Shanghai municipal health commission (No. 201640029)； STCSM (No.19ZR1446000). We gratefully acknowledge the valuable suggestions from Dr. Ning Ding, Dr. Xiaochun Dong and Dr. Weili Zhao.

REFERENCES

(1) Cameron, A. R.; Morrison, V. L.; Levin, D.; Mohan, M.; Forteath, C.; Beall, C.; McNeilly, A. D.; Balfour, D. J.; Savinko, T.; Wong, A. K.; Viollet, B.; Sakamoto, K.; Fagerholm, S. C.; Foretz, M.; Lang, C. C.; Rena, G. Anti-Inflammatory Effects of Metformin Irrespective of Diabetes Status. *Circ. Rec.* **2016**, *119*, 652-665.

(2) He, S.; Sharpless, N. E. Senescence in Health and Disease. *Cell* **2017**, *169*, 1000-1011.

(3) Ocampo, A.; Reddy, P.; Martinez-Redondo, P.; Platero-Luengo, A.; Hatanaka, F.; Hishida, T.; Li, M.; Lam, D.; Kurita, M.; Beyret, E.; Araoka, T.; Vazquez-Ferrer, E.; Donoso, D.; Roman, J. L.; Xu, J.; Rodriguez Esteban, C.; Nunez, G.; Nunez Delicado, E.; Campistol, J. M.; Guillen, I.; Guillen, P.; Izpisua Belmonte, J. C. In Vivo Amelioration of Age-Associated Hallmarks by Partial Reprogramming. *Cell* **2016**, *167*, 1719-1733 e12.

(4) Shirakabe, A.; Ikeda, Y.; Sciarretta, S.; Zablocki, D. K.; Sadoshima, J. Aging and Autophagy in the Heart. *Circ. Rec.* **2016**, *118*, 1563-1576.

(5) Childs, B. G.; Durik, M.; Baker, D. J.; van Deursen, J. M. Cellular senescence in aging and age-related disease: from mechanisms to therapy. *Nat. Med.* **2015**, *21*, 1424-1435.

(6) Demaria, M.; O'Leary, M. N.; Chang, J.; Shao, L.; Liu, S.; Alimirah, F.; Koenig, K.; Le, C.; Mitin, N.; Deal, A. M.; Alston, S.; Academia, E. C.; Kilmarx, S.; Valdovinos, A.; Wang, B.; de Bruin, A.; Kennedy, B. K.; Melov, S.; Zhou, D.; Sharpless, N. E.; Muss, H.; Campisi, J. Cellular Senescence Promotes Adverse Effects of Chemotherapy and Cancer Relapse. *Cancer Discov.* **2017**, *7*, 165-176.

(7) Jeon, O. H.; Kim, C.; Laberge, R. M.; Demaria, M.; Rathod, S.; Vasserot, A. P.; Chung, J. W.; Kim, D. H.; Poon, Y.; David, N.; Baker, D. J.; van Deursen, J. M.; Campisi, J.; Elisseeff, J. H. Local clearance of senescent cells attenuates the development of post-traumatic osteoarthritis and creates a pro-regenerative environment. *Nat. Med.* **2017**, *23*, 775-781.

(8) Munoz-Espin, D.; Serrano, M. Cellular senescence: from physiology to pathology. *Nat. Rev. Mol. Cell Biol.* **2014**, *15*, 482-496.

(9) Bennett, M. R.; Sinha, S.; Owens, G. K. Vascular Smooth Muscle Cells in Atherosclerosis. *Circ. Res.* **2016**, *118*, 692-702.

(10) Childs, B. G.; Baker, D. J.; Wijshake, T.; Conover, C. A.; Campisi, J.; van Deursen, J. M. Senescent intimal foam cells are deleterious at all stages of atherosclerosis. *Science* **2016**, *354*, 472-477.

(11) Gimbrone, M. A., Jr.; Garcia-Cardena, G. Endothelial Cell Dysfunction and the Pathobiology of Atherosclerosis. *Circ. Res.* **2016**, *118*, 620-636.

(12) Gistera, A.; Hansson, G. K. The immunology of atherosclerosis. *Nat. Rev. Nephrol.* **2017**, *13*, 368-380.

(13) Kunieda, T.; Minamino, T.; Nishi, J.; Tateno, K.; Oyama, T.; Katsuno, T.; Miyauchi, H.; Orimo, M.; Okada, S.; Takamura, M.; Nagai, T.; Kaneko, S.; Komuro, I. Angiotensin II induces premature senescence of vascular smooth muscle cells and accelerates the development of atherosclerosis via a p21-dependent pathway. *Circulation* **2006**, *114*, 953-960.

(14) Ross, R. Atherosclerosis--an inflammatory disease. *N. Engl. J. Med.* **1999**, *340*, 115-126.

(15) Tabas, I.; Garcia-Cardena, G.; Owens, G. K. Recent insights into the cellular biology of atherosclerosis. *J. Cell Biol.* **2015**, *209*, 13-22.

(16) Ding, J.; Wang, Y.; Ma, M.; Zhang, Y.; Lu, S.; Jiang, Y.; Qi, C.; Luo, S.; Dong, G.; Wen, S.; An, Y.; Gu, N. CT/fluorescence dual-modal nanoemulsion platform for investigating atherosclerotic plaques. *Biomaterials* **2013**, *34*, 209-216.

(17) Saba, L.; Sanfilippo, R.; Montisci, R.; Mallarini, G. Carotid artery wall thickness: comparison between sonography and multi-detector row CT angiography. *Neuroradiology* **2010**, *52*, 75-82.

(18) Toussaint, J. F.; LaMuraglia, G. M.; Southern, J. F.; Fuster, V.; Kantor, H. L. Magnetic resonance images lipid, fibrous, calcified, hemorrhagic, and thrombotic components of human atherosclerosis in vivo. *Circulation* **1996**, *94*, 932-938.

(19) Greco, A.; Mancini, M.; Gargiulo, S.; Gramanzini, M.; Claudio, P. P.; Brunetti, A.; Salvatore, M. Ultrasound biomicroscopy in small animal research: applications in molecular and preclinical imaging. *J. Biomed. Biotechnol.* **2012**, *2012*, 519238.

(20) Wikstrom, J.; Gronros, J.; Bergstrom, G.; Gan, L. M. Functional and morphologic imaging of coronary atherosclerosis in living mice using high-resolution color Doppler echocardiography and ultrasound biomicroscopy. *J. Am. Coll. Cardiol.* **2005**, *46*, 720-727.

(21) Chen, X.; Jin, Q.; Wu, L.; Tung, C.; Tang, X. Synthesis and unique photoluminescence properties of nitrogen-rich quantum dots and their applications. *Angew. Chem. Int. Ed.* **2014**, *53*, 12542-12547.

(22) Niu, L. Y.; Guan, Y. S.; Chen, Y. Z.; Wu, L. Z.; Tung, C. H.; Yang, Q. Z. BODIPY-based ratiometric fluorescent sensor for highly selective detection of glutathione over cysteine and homocysteine. *J. Am. Chem. Soc.* **2012**, *134*, 18928-18931.

(23) Peng, H. Q.; Niu, L. Y.; Chen, Y. Z.; Wu, L. Z.; Tung, C. H.; Yang, Q. Z. Biological Applications of Supramolecular Assemblies Designed for Excitation Energy Transfer. *Chem. Rev.* **2015**, *115*, 7502-7542.

(24) Peng, H. Q.; Sun, C. L.; Niu, L. Y.; Chen, Y. Z.; Wu, L. Z.; Tung, C. H.; Yang, Q. Z. Supramolecular Polymeric Fluorescent Nanoparticles Based on Quadruple Hydrogen Bonds. *Adv. Funct. Mater.* **2016**, *26*, 5483-5489.

(25) Shi, B.; Yan, Q.; Tang, J.; Xin, K.; Zhang, J.; Zhu, Y.; Xu, G.; Wang, R.; Chen, J.; Gao, W.; Zhu, T.; Shi, J.; Fan, C.; Zhao, C.; Tian, H. Hydrogen Sulfide-Activatable Second Near-Infrared Fluorescent Nanoassemblies for Targeted Photothermal Cancer Therapy. *Nano Lett.* **2018**, *18*, 6411-6416.

(26) Wang, F.; Xu, G.; Gu, X.; Wang, Z.; Wang, Z.; Shi, B.; Lu, C.; Gong, X.; Zhao, C. Realizing highly chemoselective detection of H_2S in vitro and in vivo with fluorescent probes inside core-shell silica nanoparticles. *Biomaterials* **2018**, *159*, 82-90.

(27) Wang, R.; Dong, K.; Xu, G.; Shi, B.; Zhu, T.; Shi, P.; Guo, Z.; Zhu, W. H.; Zhao, C. Activatable near-infrared emission-guided on-demand administration of photodynamic anticancer therapy with a theranostic nanoprobe. *Chem. Sci.* **2019**, *10*, 2785-2790.

(28) Xu, G.; Yan, Q.; Lv, X.; Zhu, Y.; Xin, K.; Shi, B.; Wang, R.; Chen, J.; Gao, W.; Shi, P.; Fan, C.; Zhao, C.; Tian, H. Imaging of Colorectal Cancers Using Activatable Nanoprobes with Second Near-Infrared Window Emission. *Angew. Chem. Int. Ed.* **2018**, *57*, 3626-3630.

(29) Chen, H. Z.; Wang, F.; Gao, P.; Pei, J. F.; Liu, Y.; Xu, T. T.; Tang, X.; Fu, W. Y.; Lu, J.; Yan, Y. F.; Wang, X. M.; Han, L.; Zhang, Z. Q.; Zhang, R.; Zou, M. H.; Liu, D. P. Age-Associated Sirtuin 1

Reduction in Vascular Smooth Muscle Links Vascular Senescence and Inflammation to Abdominal Aortic Aneurysm. *Circ. Res.* **2016**, *119*, 1076-1088.

(30) Daugherty, A.; Manning, M. W.; Cassis, L. A. Angiotensin II promotes atherosclerotic lesions and aneurysms in apolipoprotein E-deficient mice. *J. Clin. Invest.* **2000**, *105*, 1605-1612.

(31) Minamino, T.; Komuro, I. Vascular cell senescence: contribution to atherosclerosis. *Circ. Res.* **2007**, *100*, 15-26.

(32) Weiss, D.; Kools, J. J.; Taylor, W. R. Angiotensin II-induced hypertension accelerates the development of atherosclerosis in apoE-deficient mice. *Circulation* **2001**, *103*, 448-454.

(33) Debacq-Chainiaux, F.; Erusalimsky, J. D.; Campisi, J.; Toussaint, O. Protocols to detect senescence-associated beta-galactosidase (SA-betagal) activity, a biomarker of senescent cells in culture and in vivo. *Nat. Protoc.* **2009**, *4*, 1798-1806.

(34) Sharpless, N. E.; Sherr, C. J. Forging a signature of in vivo senescence. *Nat. Rev. Cancer* **2015**, *15*, 397-408.

(35) Kim, E.-J.; Podder, A.; Maiti, M.; Lee, J. M.; Chung, B. G.; Bhuniya, S. Selective monitoring of vascular cell senescence via β-Galactosidase detection with a fluorescent chemosensor. *Sens. Actuators. B* **2018**, *274*, 194-200.

(36) Lee, H. W.; Heo, C. H.; Sen, D.; Byun, H. O.; Kwak, I. H.; Yoon, G.; Kim, H. M. Ratiometric two-photon fluorescent probe for quantitative detection of beta-galactosidase activity in senescent cells. *Anal. Chem.* **2014**, *86*, 10001-10005.

(37) Lozano-Torres, B.; Galiana, I.; Rovira, M.; Garrido, E.; Chaib, S.; Bernardos, A.; Munoz-Espin, D.; Serrano, M.; Martinez-Manez, R.; Sancenon, F. An OFF-ON Two-Photon Fluorescent Probe for Tracking Cell Senescence in vivo. *J. Am. Chem. Soc.* **2017**, *139*, 8808-8811.

(38) Zhang, J.; Li, C.; Dutta, C.; Fang, M.; Zhang, S.; Tiwari, A.; Werner, T.; Luo, F. T.; Liu, H. A novel near-infrared fluorescent probe for sensitive detection of beta-galactosidase in living cells. *Anal. Chim. Acta* **2017**, *968*, 97-104.

(39) Chen, L.; Nakano, K.; Kimura, S.; Matoba, T.; Iwata, E.; Miyagawa, M.; Tsujimoto, H.; Nagaoka, K.; Kishimoto, J.; Sunagawa, K.; Egashira, K. Nanoparticle-mediated delivery of pitavastatin into lungs ameliorates the development and induces regression of monocrotaline-induced pulmonary artery hypertension. *Hypertension* **2011**, *57*, 343-350.

(40) Katsuki, S.; Matoba, T.; Nakashiro, S.; Sato, K.; Koga, J.; Nakano, K.; Nakano, Y.; Egusa, S.; Sunagawa, K.; Egashira, K. Nanoparticle-mediated delivery of pitavastatin inhibits atherosclerotic plaque destabilization/rupture in mice by regulating the recruitment of inflammatory monocytes. *Circulation* **2014**, *129*, 896-906.

(41) Bugaut, A.; Jantos, K.; Wietor, J. L.; Rodriguez, R.; Sanders, J. K.; Balasubramanian, S. Exploring the differential recognition of DNA G-quadruplex targets by small molecules using dynamic combinatorial chemistry. *Angew. Chem. Int. Ed.* **2008**, *47*, 2677-2680.

(42) Bindels, D. S.; Haarbosch, L.; van Weeren, L.; Postma, M.; Wiese, K. E.; Mastop, M.; Aumonier, S.; Gotthard, G.; Royant, A.; Hink, M. A.; Gadella, T. W., Jr. mScarlet: a bright monomeric red fluorescent protein for cellular imaging. *Nat. Methods* **2017**, *14*, 53-56.

(43) Chen, H.; Tang, Y.; Ren, M.; Lin, W. Single near-infrared fluorescent probe with high- and low-sensitivity sites for sensing different concentration ranges of biological thiols with distinct modes of fluorescence signals. *Chem. Sci.* **2016**, *7*, 1896-1903.

(44) Liu, Y.; Tan, J.; Zhang, Y.; Zhuang, J.; Ge, M.; Shi, B.; Li, J.; Xu, G.; Xu, S.; Fan, C.; Zhao, C. Visualizing glioma margins by real-time tracking of gamma-glutamyltranspeptidase activity. *Biomaterials* **2018**, *173*, 1-10.

(45) Miao, Q.; Lyu, Y.; Ding, D.; Pu, K. Semiconducting Oligomer Nanoparticles as an Activatable Photoacoustic Probe with Amplified Brightness for In Vivo Imaging of pH. *Adv. Mater.* **2016**, *28*, 3662-3668.

(46) Wang, F.; Zhou, L.; Zhao, C.; Wang, R.; Fei, Q.; Luo, S.; Guo, Z.; Tian, H.; Zhu, W. H. A dual-response BODIPY-based fluorescent probe for the discrimination of glutathione from cystein and homocystein. *Chem. Sci.* **2015**, *6*, 2584-2589.

(47) Wu, P.; Hou, X.; Xu, J. J.; Chen, H. Y. Ratiometric fluorescence, electrochemiluminescence, and photoelectrochemical chemo/bio-sensing based on semiconductor quantum dots. *Nanoscale* **2016**, *8*, 8427-8442.

(48) Xu, R.; Wang, Y.; Duan, X.; Lu, K.; Micheroni, D.; Hu, A.; Lin, W. Nanoscale Metal-Organic Frameworks for Ratiometric Oxygen Sensing in Live Cells. *J. Am. Chem. Soc.* **2016**, *138*, 2158-2161.

(49) Zhao, C.; Zhang, X.; Li, K.; Zhu, S.; Guo, Z.; Zhang, L.; Wang, F.; Fei, Q.; Luo, S.; Shi, P.; Tian, H.; Zhu, W. H. Forster Resonance Energy Transfer Switchable Self-Assembled Micellar Nanoprobe: Ratiometric Fluorescent Trapping of Endogenous H_2S Generation via Fluvastatin-Stimulated Upregulation. *J. Am. Chem. Soc.* **2015**, *137*, 8490-8498.

(50) Bonomini, F.; Rodella, L. F.; Moghadasian, M.; Lonati, C.; Rezzani, R. Apolipoprotein E deficiency and a mouse model of accelerated liver aging. *Biogerontology* **2013**, *14*, 209-220.

(51) Sookoian, S.; Pirola, C. J. Non-alcoholic fatty liver disease is strongly associated with carotid atherosclerosis: a systematic review. *J. Hepatol.* **2008**, *49*, 600-607.

(52) Tsukamoto, K.; Tangirala, R.; Chun, S. H.; Pure, E.; Rader, D. J. Rapid regression of atherosclerosis induced by liver-directed gene transfer of ApoE in ApoE-deficient mice. *Arterioscler. Thromb. Vasc. Biol.* **1999**, *19*, 2162-2170.

TOC